



Effect of transition metal substitution on structural and dielectric properties of $\text{Mg}_{0.5}\text{Zn}_{0.5-x}\text{Cr}_x\text{Co}_2\text{O}_4$ ($0.0 \leq x \leq 0.5$) cobaltite

Pallavi Saxena¹ · P. Choudhary¹ · A. Yadav^{1,2} · V. N. Rai¹ · M. Varshney¹ · A. Mishra¹

Received: 23 October 2018 / Accepted: 28 February 2019 / Published online: 8 March 2019
© Springer Science+Business Media, LLC, part of Springer Nature 2019

Abstract

We report the impact of Cr ion doping on structural and dielectric properties of $\text{Mg}_{0.5}\text{Zn}_{0.5-x}\text{Cr}_x\text{Co}_2\text{O}_4$ ($0.0 \leq x \leq 0.5$). All the samples were prepared by high-temperature solid-state reaction route. X-ray diffraction patterns reveal that $\text{Mg}_{0.5}\text{Zn}_{0.5-x}\text{Cr}_x\text{Co}_2\text{O}_4$ ($0.0 \leq x \leq 0.5$) crystallizes into more than one phase. Rietveld analysis of Synchrotron-based X-ray diffraction also confirms the existence of secondary phases corresponding to the cubic structure with $Fd-3m$ and $Fm3m$ space group. Scanning electron microscopy (SEM) images confirm the growth in grain size as a result of high sintering temperature. The FTIR spectra of doped cobaltites show two strong peaks at ~ 665 and 563 cm^{-1} due to the presence of metal–oxygen bond. Variation in the dielectric constant and dielectric loss with frequency have also been investigated. Both decreases with increasing frequency of the applied alternating field and becomes constant at high frequencies that signify the substantial role of interfacial polarisation. It is also noted that the material having the smallest crystallite size ($\sim 29.16 \text{ nm}$) has high dielectric constant ($\sim 1.07 \times 10^5$) value. Cole–Cole plot indicates that all the samples of cobaltite show dominant grain capacitance.

1 Introduction

An increase in energy consumption and rapid technological development offers an opportunity for the development of new energy storage devices, having high efficiency along with environmental-friendly and safe energy storage devices [1, 2]. In this perspective, supercapacitor (electrochemical capacitors or ultracapacitors) is widely recognized due to its fast charge–discharge property, high power density, long cycle life and outstanding cycle performance [3]. Usually, the performance of supercapacitor devices is determined based on its electrode materials. However, the physical and chemical properties of capacitors can be modified by several amalgamations of cations in mixed transition metal oxides [4]. The cobalt-based mixed transition metal oxides (Co_3O_4) are most promising and favorable substitutes for supercapacitor and energy storage devices due to its electrochemical

stability, large surface area and high conductivity among the numerous electrode materials [5].

Co_3O_4 in bulk form is antiferromagnetic in nature with the Neel temperature $T_N \approx 290 \text{ K}$, whereas in nano form little ferromagnetic nature is observed. Optical studies of Co_3O_4 show that it is a p -type semiconductor with direct band gaps at 1.48 and 2.19 eV, among the various transition metal oxides [6]. Co_3O_4 has three well-known valence states such as the cobaltous oxide (CoO), the cobaltic oxide (Co_2O_3), and the cobalt cobaltite (Co_3O_4). The most stable phase in the cobalt oxide system is a mixed valence compound ($\text{Co}^{2+}\text{Co}_2^{3+}\text{O}_4$).

$\text{Co}^{2+}\text{Co}_2^{3+}\text{O}_4$ shows a normal spinel structure, in which the tetrahedral sites are occupied by Co^{2+} ion and octahedral sites are occupied by Co^{3+} ion. In fact, the divalent Co^{2+} can be further coordinated to the O anions up to a maximum of six as in the CoO phase. The Co^{2+} ions occupy octahedral sites formed by six O anions (rock salt structure). In recent years, several efforts have been made to fabricate a systems of cobalt oxide with tunable physical and chemical properties for broad range of applications, among which transition metal doping (such as $\text{A}_x\text{Co}_{3-x}\text{O}_4$; $\text{A} = \text{Zn, Mn, Ni, Fe, etc.}$) is a promising and efficient route to improve the electrical behavior of Co_3O_4 [7].

ZnCo_2O_4 anode materials also have remarkable electrochemical reaction mechanism toward lithium ions. Since Zn

✉ Pallavi Saxena
pallaviphy12@gmail.com

¹ Materials Science Laboratory, School of Physics, Vigyan Bhavan, Devi Ahilya University, Khandwa Road Campus, Indore 452001, India

² Department of Physics, Medi-Caps University, Pigdamber, Indore 453331, India

and Co both are electrochemically actives toward lithium and their complementary behavior can enhance the performance of lithium-storage [8]. In consequence, the theoretical capacity of ZnCo_2O_4 is superior compared to most of the other cobaltite (ACo_2O_4 [A = Mg, Cu, and Ni]) [9]. But like other mixed transition metal oxides anode materials, ZnCo_2O_4 also undergoes short cycling life. Recently, magnesium spinel oxides (such as MgCo_2O_4) were proposed as a promising electrode material for magnesium rechargeable batteries (MRBs). The spinel lattice transforms into a rock-salt phase through the insertion of magnesium ions in MgCo_2O_4 [10]. Due to the low conductivity of magnesium ions in the solid phase, improvements in the insertion process are of great importance in order to enhance the electrochemical properties of MRBs [11].

We have noted that the earlier observed magnetic and dielectric response of ZnCo_2O_4 is not good as compare to the other cobaltites. However, the dielectric constant of Co_3O_4 is reported as $\sim 6.17 \times 10^4$ [12]. It is also known that the cobaltite doped with zinc ion leads to a substantial improvement in the thermal stability of the structure. Doped cobaltite received theoretical and practical attention because of their high activity in the low-temperature [13]. Thus it is important to investigate the dielectric behavior of mixed Mg and ZnCo_2O_4 . Spinel as ferrites, chromites, cobaltites, aluminates and nickelates possess unique dielectric properties and are efficiently used for high-frequency device applications. Normally the high-frequency devices require low dielectric loss ($\tan \delta$) because its lower value indicates higher efficiency and lower noise in the device. No observations are reported for mixed Mg and Zn cobalt oxide, whereas MgCo_2O_4 , ZnCo_2O_4 , and CrCo_2O_4 show the cubic spinel structure (with $Fd3m$ space group).

The main aim of this paper is to synthesize bulk ceramics $\text{Mg}_{0.5}\text{Zn}_{0.5-x}\text{Cr}_x\text{Co}_2\text{O}_4$ ($0.0 \leq x \leq 0.5$) via solid-state reaction route technique in order to enhance and optimize its dielectric properties. Applicability of these materials as supercapacitor is also discussed.

2 Experimental details

Cr doped Mg–Zn Cobaltites samples of $\text{Mg}_{0.5}\text{Zn}_{0.5-x}\text{Cr}_x\text{Co}_2\text{O}_4$ ($0.0 \leq x \leq 0.5$) were prepared by the conventional solid-state reaction technique using MgO (96%), ZnO (99.9%), Cr_2O_3 (98%), and Co_3O_4 (70%) as starting materials. The stoichiometric mixture of the oxide powders was thoroughly mixed using mortar pestle and then fired at 1100 °C for 12 h. The product was reground and fired again at 1150 °C (12 h) to improve its homogeneity.

X-ray diffraction (XRD) patterns of the samples were obtained at room temperature using an X-ray diffractometer (Model D-800, Dianocorporation-USA) Bruker D8 Advance

over the angular range 10–80° working at 40 kV voltage and 40 mA current with $\text{CuK}\alpha_1$ (1.5406 Å) radiation source. The Synchrotron X-ray diffraction (SXR) was obtained using angle-dispersive X-ray diffraction (ADXRD) beamline (BL-12) at Indus-2 synchrotron source (RRCAT, Indore, India), where the wavelength of X-ray was (0.8042 Å). The powder samples were pelletized into circular disk size 10 × 1 mm at 8 tone pressure, using a hydraulic press. The pellets were further sintered at 1200 °C for 15 h. Surface morphology of the sintered pellets has been examined by scanning electron microscope [SEM: JEOL-JSM-5600] coupled with energy dispersive spectrometer (INCA Oxford). Room temperature Fourier transform infrared (FTIR) spectra were recorded as ATR based Frontier Perkin-Elmer (SP 10 STD) in the frequency range 4000–400 cm^{-1} .

Sintered pellets were coated with high-purity silver paste on adjacent faces as electrodes and then dried for few hours to make the parallel plate capacitor geometry for dielectric measurements. The room temperature dielectric measurement was performed using impedance analyzer (model—Wayne Kerr 6500B) working in the frequency range of 20 Hz to 120 MHz and in the *ac* voltage range from 10 mV to 1 V.

3 Results and discussion

3.1 X-ray diffraction analysis

XRD pattern of $\text{Mg}_{0.5}\text{Zn}_{0.5-x}\text{Cr}_x\text{Co}_2\text{O}_4$ ($0.0 \leq x \leq 0.5$) ceramics are depicted in Fig. 1. The diffraction patterns reveal that $\text{Mg}_{0.5}\text{Zn}_{0.5-x}\text{Cr}_x\text{Co}_2\text{O}_4$ ($0.0 \leq x \leq 0.5$) crystallizes in more than one phase. The magnified view of XRD shows the splitting of (111) peak with an increase in the content of Cr,

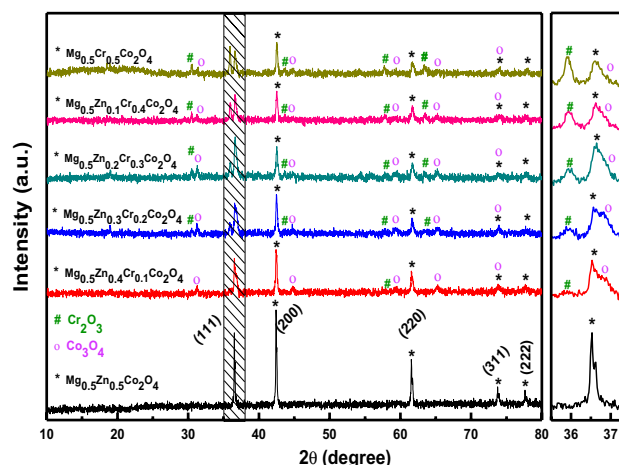


Fig. 1 X-ray diffraction patterns of $\text{Mg}_{0.5}\text{Zn}_{0.5-x}\text{Cr}_x\text{Co}_2\text{O}_4$ ($0.0 \leq x \leq 0.5$)

which may be due to the existence of more than one phase. Lattice distortions may also be occurring in the samples with higher Cr composition. These lattice distortions showed possible influence in lattice parameter of Cr-substituted Mg–Zn Cobaltite compositions, similar results have been reported earlier in Eu-substituted BiFeO₃ [14]. The structural parameters of Mg_{0.5}Zn_{0.5-x}Cr_xCo₂O₄ (0.0 ≤ x ≤ 0.5) obtained by the XRD patterns at room temperature are tabulated in Table 1.

The average crystallite sizes in various samples were calculated using Scherrer's equation [15] $t = 0.9 \lambda / \beta \cos \theta$, where λ is the X-ray wavelength employed, θ is the diffraction angle and β is full width at half maximum (FWHM). The obtained values of crystallites sizes are ~43, 36, 34, 29, 33 and 33 nm for $x = 0.0, x = 0.1, x = 0.2, x = 0.3, x = 0.4$ and $x = 0.5$, respectively. We further calculate microstrain ($\epsilon = \beta / 4 \tan \theta$), where β is FWHM, θ is the diffraction angle and λ is the X-ray wavelength employed. The presence of induced microstrain in prepared samples also include lattice deformation, stress and grain barriers in the form of oxygen vacancy. The dislocation density was also calculated using the equation $\delta = 1/t^2$, where t is the crystallite size [16]. Since δ is the measure of the amount of defects in a crystal, the higher values of δ obtained in the present study confirmed the presence of a defect.

Table 2 lists relative density. Relative densities were calculated as the ratio of the experimental to the theoretical densities of samples. Experimental densities were determined by the Archimedes method and the theoretical

densities were calculated from the simple rule of mixtures. X-ray diffraction confirms the existence of secondary phases corresponding to the cubic structure with *Fd-3m* and *Fm3m* space group. It might be due to the coexistence of spinel-type (Cr₂O₃ and Co₃O₄) and rocksalt-type (Mg_{0.5}Zn_{0.5}Co₂O₄) structures.

SXRD is a powerful probe to identify the grain-size-induced line broadening due to high angular resolution ~0.06°. On the other hand, laboratory XRD probes a limited resolution. Apart from this, the high intensity available at a synchrotron source enables us to record a diffraction pattern in less time with sufficient count rates; such a time resolution cannot be reached with a laboratory diffractometer. Henceforth, to know the structural phase stability in the samples, SXRD pattern of Mg_{0.5}Zn_{0.5-x}Cr_xCo₂O₄ ($x = 0.0, 0.3, 0.5$) are recorded and shown in Fig. 2. The calculation of the crystallite size was obtained using Scherer formula. It shows the reduced value of particle size when compared to lab XRD, which may be ascribed to the noisy and less effective lab XRD data compared to the SXRD. The detailed analysis of measured SXRD patterns of the samples was based on the Rietveld refinement (using the FullPROF software) [17] as displayed in Fig. 3. The refinement was performed in the Rietveld method to minimize the difference between the observed and calculated powder diffraction patterns. The pseudo-voigt analytical function was used to fit the experimental peak. The refined (SXRD) lattice

Table 1 Structural parameter and force constant of Mg_{0.5}Zn_{0.5-x}Cr_xCo₂O₄ (0.0 ≤ x ≤ 0.5)

Material	Crystallite size ± 0.001 (nm)	Crystallite size from SXRD ± 0.001 (nm)	Microstrain	Dislocation density (line/m ²)	Force constant (dyne/cm)	
					$k_t \times 10^5$	$k_o \times 10^5$
Mg _{0.5} Zn _{0.5} Co ₂ O ₄	43.33	42.48	1.38×10^{-1}	5.32×10^{14}	3.25	2.33
Mg _{0.5} Zn _{0.4} Cr _{0.1} Co ₂ O ₄	36.66	–	3.92×10^{-3}	7.43×10^{14}	3.23	2.27
Mg _{0.5} Zn _{0.3} Cr _{0.2} Co ₂ O ₄	34.41	–	4.26×10^{-3}	8.44×10^{14}	3.22	2.26
Mg _{0.5} Zn _{0.2} Cr _{0.3} Co ₂ O ₄	29.16	28.00	5.53×10^{-3}	11.75×10^{14}	3.19	2.23
Mg _{0.5} Zn _{0.1} Cr _{0.4} Co ₂ O ₄	33.35	–	4.32×10^{-3}	8.98×10^{14}	3.16	2.22
Mg _{0.5} Cr _{0.5} Co ₂ O ₄	33.05	27.33	4.27×10^{-3}	9.15×10^{14}	3.14	2.20

Table 2 Details of Rietveld refined SXRD parameters for Mg_{0.5}Zn_{0.5-x}Cr_xCo₂O₄ ($x = 0.0, 0.3, 0.5$)

Material	Space group	Wt (%)	Lattice parameter $a \pm 0.001$ (Å)	Relative density (%)	χ^2	
Mg _{0.5} Zn _{0.5} Co ₂ O ₄	<i>Fm3m</i>	MgZnCo ₂ O ₄	100	4.288	22.41	2.79
Mg _{0.5} Zn _{0.2} Cr _{0.3} Co ₂ O ₄	<i>Fm3m</i>	MgZnCrCo ₂ O ₄	23.52	4.278	62.21	1.32
	<i>Fd-3m</i>	Cr ₂ O ₃	27.94	8.338		
	<i>Fd-3m</i>	Co ₃ O ₄	48.55	8.143		
Mg _{0.5} Cr _{0.5} Co ₂ O ₄	<i>Fm3m</i>	MgCrCo ₂ O ₄	27.88	4.294	62.57	3.45
	<i>Fd-3m</i>	Cr ₂ O ₃	25.25	8.184		
	<i>Fd-3m</i>	Co ₃ O ₄	46.87	8.377		

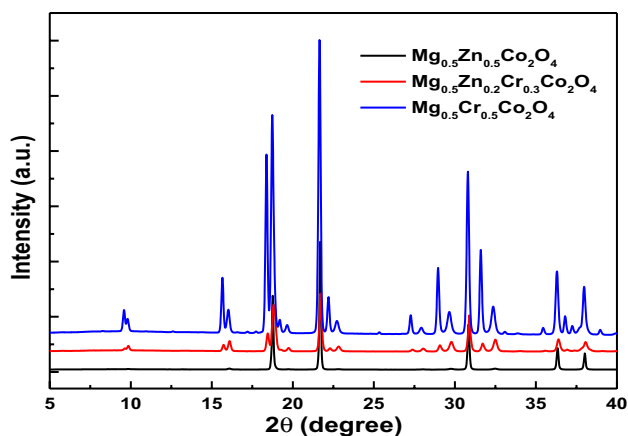


Fig. 2 Synchrotron X-ray diffraction (SXR) patterns of $\text{Mg}_{0.5}\text{Zn}_{0.5-x}\text{Cr}_x\text{Co}_2\text{O}_4$ ($x=0.0, 0.3, 0.5$)

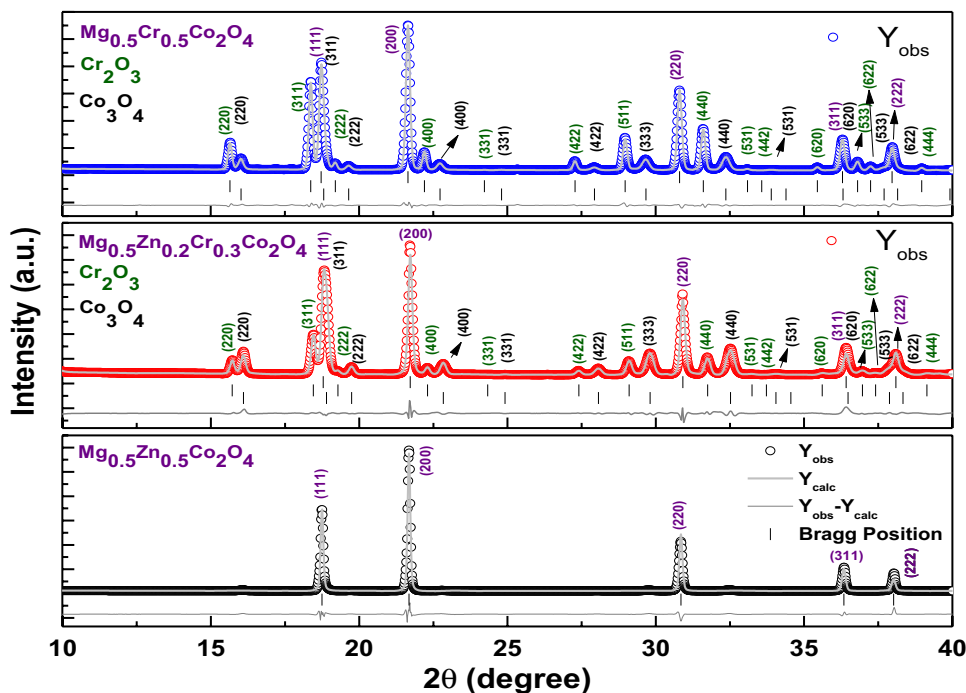
parameters, weight fraction and the goodness of fit (χ^2) of $\text{Mg}_{0.5}\text{Zn}_{0.5-x}\text{Cr}_x\text{Co}_2\text{O}_4$ ($x=0.0, 0.3, 0.5$) samples are listed in Table 2.

From refined SXR we see that the peaks corresponding to $\text{Mg}_{0.5}\text{Zn}_{0.5}\text{Co}_2\text{O}_4$ ceramics are indexed to cubic structure associated with a space group of $Fm\bar{3}m$ [18]. In Mg–Zn cobaltite doped with Cr, cobaltite phase is unstable and degrades into secondary phases, such as MgO, Cr_2O_3 and Co_3O_4 (rocksalt-type and spinel-type structures). These phases correspond to cubic symmetry with space group $Fm\bar{3}m$ and $Fd\bar{3}m$. The weight fraction of secondary phases strongly supports the formation of the composite

phase. We also note that all the peaks are shifted slightly towards the lower angle as the concentration of Cr is increased. It is attributed to the compression strain induced in the structure due to the difference in ionic radii of Zn^{2+} (0.74 Å [19]) and Cr^{2+} (0.80 Å [19]) ions [20, 21].

The detailed morphology of $\text{Mg}_{0.5}\text{Zn}_{0.5-x}\text{Cr}_x\text{Co}_2\text{O}_4$ (0.0, 0.2, 0.3 and 0.5) cobaltites was obtained by scanning electron microscopy (SEM) with the resolution of 10 μm as shown in Fig. 4. All the samples were sintered at 1200 °C for 15 h, provide high densification and excellent crystallinity. Higher sintering temperature yields larger grain size due to interdiffusion of mass that reduces the strain. The SEM images show a group of bright and dark regions. The image processing software (Image J) developed by the National Institute of Health is used for particle size analysis [22, 23]. Inset of Fig. 4 shows the size distribution of the samples. All the images show well-defined crystals with different shapes. It is observed that the average grain sizes vary from 2 to 4 μm for all the samples. It is noted that the average grain size of the compositions obtained from SEM is larger than the crystallite size of the samples as calculated using XRD and SXR analysis (Table 1). This fact suggests that each grain is the resultant of agglomeration of a number of nanocrystals. The micrographs show the agglomerated grainy structure with clusters of fine particles clinging together [24]. The images also show that samples did not reach high relative density which can significantly affect the physical properties of the samples.

Fig. 3 Reitveld refinement of $\text{Mg}_{0.5}\text{Zn}_{0.5-x}\text{Cr}_x\text{Co}_2\text{O}_4$ ($x=0.0, 0.3, 0.5$)



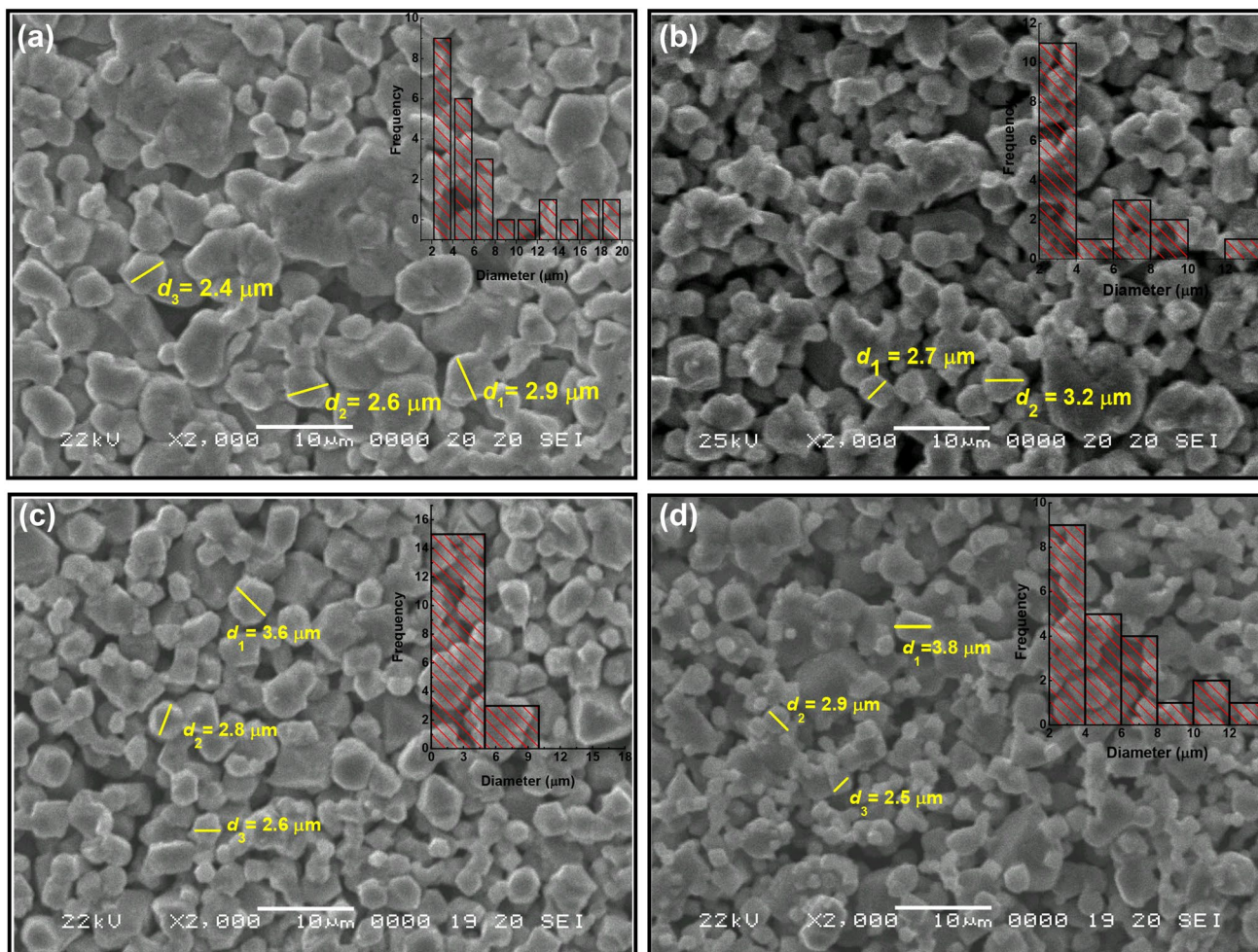


Fig. 4 SEM images of $\text{Mg}_{0.5}\text{Zn}_{0.5-x}\text{Cr}_x\text{Co}_2\text{O}_4$ ($x=0.0, 0.2, 0.3, 0.5$)

3.2 FTIR analysis

FTIR spectra of $\text{Mg}_{0.5}\text{Zn}_{0.5-x}\text{Cr}_x\text{Co}_2\text{O}_4$ ($0.0 \leq x \leq 0.5$) cobaltites in the range of $3500\text{--}500\text{ cm}^{-1}$ are depicted in Fig. 5. The calcined cobaltites samples produce two strong peaks with a medium amplitude at around 665 and 563 cm^{-1} that are assigned to the stretching and vibrations of the bonds. It might be due to the presence of the metal–oxygen bond in the sample [25]. Similarly, FTIR analysis of cobalt oxide (Co_3O_4) films deposited on the stainless steel substrate is documented earlier [26]. The metal–oxygen peaks that appeared at around 563 and 665 cm^{-1} for $\text{Mg}_{0.5}\text{Zn}_{0.5}\text{Co}_2\text{O}_4$ samples are found slightly shifted towards lower wavenumber. As the Cr is introduced in the samples, the shifting in the positions of bands occurs due to change in the bond length of Co–O, which is related to changes in the surface area and surface defects due to doping [27]. The inset picture of FTIR spectra clearly shows the closer view of metal–oxygen peaks in all the samples.

The values of force constant for tetrahedral (k_t) and octahedral (k_o) sites are listed in Table 1. It is observed that both k_t and k_o decrease with increase in Cr concentration. Normally, it is expected that an increase in the bond length should lead to a decrease in the force constant. A decrease in wave number and force constant is expected with Cr substitution because of its larger ionic radius (0.80 \AA) than the displaced ion (0.74 \AA). The observed decrease in the wave numbers and force constants which are composition dependent at both the sites indicate the occupancy of chromium ions at both A and B sites [28].

But with the presence of chromium doping the force constants at the octahedral site decreased from 2.33×10^5 to 2.20×10^5 dyne/cm and at the tetrahedral site decreased from 3.25×10^5 to 3.14×10^5 dyne/cm. The change of the force constant at the tetrahedral site is 0.11 dyne/cm while the octahedral site is 0.13 dyne/cm. These results indicate that changes in the octahedral site are greater than at the tetrahedral site after doping of chromium ions [29].

Fig. 5 FTIR spectra of $\text{Mg}_{0.5}\text{Zn}_{0.5-x}\text{Cr}_x\text{Co}_2\text{O}_4$ ($0.0 \leq x \leq 0.5$) compounds

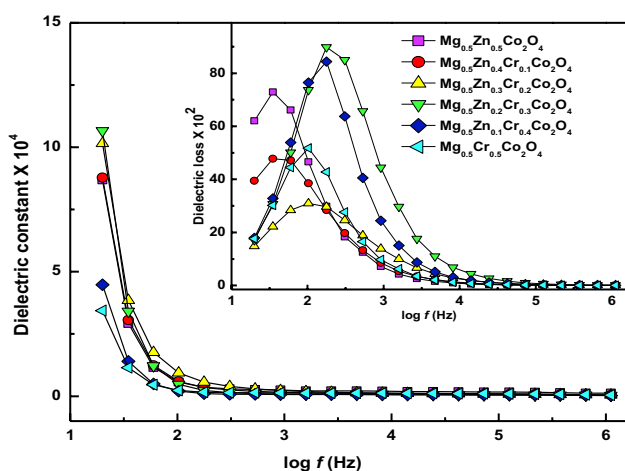
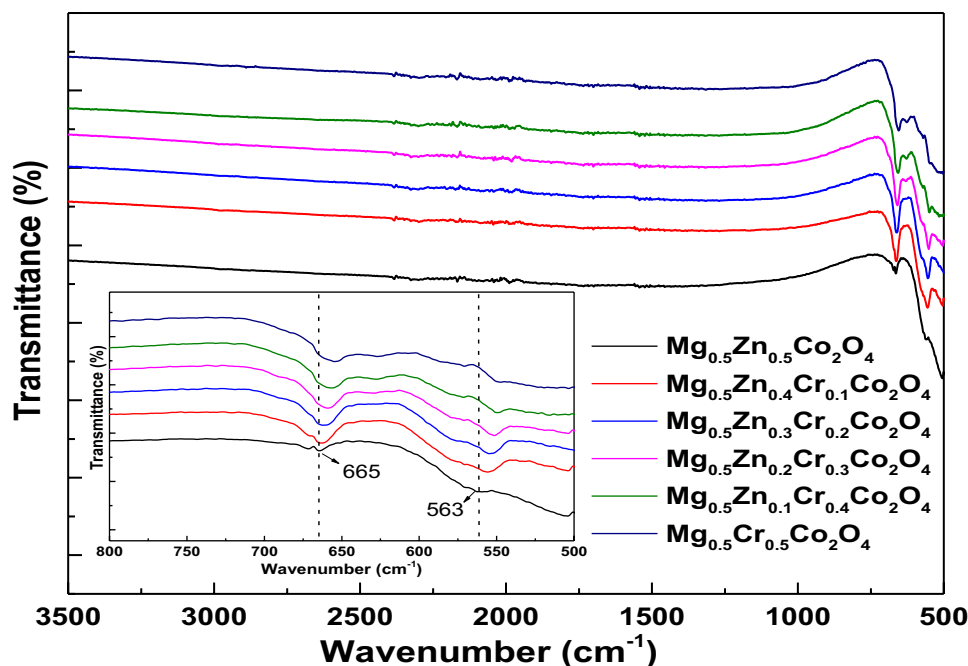


Fig. 6 Frequency dependent dielectric constant (ϵ') and (inset view) loss tangent ($\tan\delta$) of $\text{Mg}_{0.5}\text{Zn}_{0.5-x}\text{Cr}_x\text{Co}_2\text{O}_4$ ($0.0 \leq x \leq 0.5$) samples recorded at room temperature

3.3 Dielectric analysis

The effect of frequency ranging from 20 Hz to 1 MHz on dielectric constant (ϵ') and dielectric loss ($\tan\delta$) of $\text{Mg}_{0.5}\text{Zn}_{0.5-x}\text{Cr}_x\text{Co}_2\text{O}_4$ ($0.0 \leq x \leq 0.5$) cobaltite at room temperature is shown in Fig. 6. All the samples display decreasing trends of ϵ' with increasing frequency (f) from 20 Hz to 1 MHz range. The above behavior is attributed to the condition of dipoles resulting from the changes in valence states of cations and space charge polarization. As the frequency increases the space charge polarization decreases, due to ionic and dipolar polarization. Because

dipoles do not follow the path of the field and result in a low value of ϵ' at high-frequency region [30]. The conducting grains are also separated by poorly conducting grain boundaries. All the compositions exhibit a higher value of ϵ' at a lower frequency and it is associated with the conduction in $\text{Mg}_{0.5}\text{Zn}_{0.5-x}\text{Cr}_x\text{Co}_2\text{O}_4$, Cr_2O_3 and Co_3O_4 phases. This is also attributed to Maxwell–Wagner type interfacial polarization in agreement with Koop's theory [31]. The dielectric behavior in the composites can also be explained on the basis of polarization mechanism that similar to the conduction process. Because conduction in the composites beyond phase separation limits is due to the existence of different phases [32]. Since in cobaltite the rotation of $\text{Co}^{3+} \leftrightarrow \text{Co}^{4+}$ dipoles results in orientational polarization that may be visualized as an exchange of electrons between the ions and the dipoles aligning themselves with the alternating field [33]. The dielectric constant values (ϵ') at higher frequencies may be attributed to the fact that beyond a certain frequency, the electron exchange between $\text{Co}^{3+} \leftrightarrow \text{Co}^{4+}$ does not follow an alternating field.

The values of ϵ' , $\tan\delta$ and ac conductivity (σ_{ac}) are shown in Table 3. The value of ϵ' ($\sim 0.87 \times 10^5$) for $\text{Mg}_{0.5}\text{Zn}_{0.5}\text{Co}_2\text{O}_4$ increases with Cr concentration till certain value (30% Cr) and then decreases for $x > 0.3$ is found consistent with previous reports [34]. Figure 6 also explains the high dielectric constant value for $\text{Mg}_{0.5}\text{Zn}_{0.2}\text{Cr}_{0.3}\text{Co}_2\text{O}_4$ which has smallest crystallite size among all the samples. It might be due to the presence of small grains, which acts as a large insulating barrier for the mobile charge carriers. $\text{Mg}_{0.5}\text{Zn}_{0.2}\text{Cr}_{0.3}\text{Co}_2\text{O}_4$ having smallest grains gives rise to large insulation as compared

Table 3 Dielectric constant (ϵ'), loss ($\tan \delta$), ac conductivity (σ_{ac}) and β factor of $Mg_{0.5}Zn_{0.5-x}Cr_xCo_2O_4$ ($0 \leq x \leq 0.5$) at low frequency region (20 Hz) and room temperature

Compounds	ϵ'	$\tan \delta$	σ_{ac}	β
$Mg_{0.5}Zn_{0.5}Co_2O_4$	0.87×10^5	62.08×10^2	0.24	0.95
$Mg_{0.5}Zn_{0.4}Cr_{0.1}Co_2O_4$	0.89×10^5	39.42×10^2	0.16	0.97
$Mg_{0.5}Zn_{0.3}Cr_{0.2}Co_2O_4$	1.02×10^5	14.82×10^2	0.17	0.78
$Mg_{0.5}Zn_{0.2}Cr_{0.3}Co_2O_4$	1.07×10^5	17.13×10^2	0.2	0.79
$Mg_{0.5}Zn_{0.1}Cr_{0.4}Co_2O_4$	0.45×10^5	17.98×10^2	0.09	0.6
$Mg_{0.5}Cr_{0.5}Co_2O_4$	0.34×10^5	17.61×10^2	0.07	0.71

to other samples. This implies that grain and grain-boundaries play an essential role [35].

The variance in dielectric constant is also attributed to the space charge polarization due to inhomogeneous dielectric structure such as porosity, stoichiometry, and grain structure. At lower frequencies, $\tan \delta$ has some significant values and as the frequency rises its value goes to zero. This might be due to reason that charges can contribute to field orientation at low frequencies henceforth we get a low dielectric loss at high-frequency regime [36]. We observe dielectric relaxation peak in dielectric loss behavior for all the prepared ceramics, which can be due to the resonance effect. When the frequency of the external ac field is equal to the hopping frequency of the charge carriers, the maximum electrical energy is transferred to the oscillating ions and we observe a peak in power loss. Similar behavior in the case of Mn-substituted Ni–Zn ferrites was observed [37]. The dielectric relaxation peak has also shifted towards the lower frequency with the increasing crystallite size.

Figure 7 shows variation in the measured σ_{ac} of $Mg_{0.5}Zn_{0.5-x}Cr_xCo_2O_4$ ($0.0 \leq x \leq 0.5$) cobaltite samples with the frequency of the applied alternating field (f) from 20 Hz to 1 MHz frequency. It has been observed that σ_{ac}

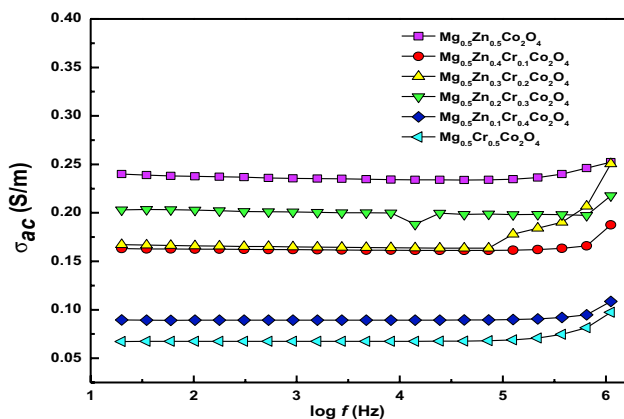


Fig. 7 Plot of ac conductivity with the frequency of $Mg_{0.5}Zn_{0.5-x}Cr_xCo_2O_4$ ($0.0 \leq x \leq 0.5$) at room temperature

remains constant up to certain frequency ($\sim 10^5$ Hz) and then increases with frequency and it could be explained on the basis of Koop's model [38]. Conductivity at low frequency is due to the grain boundaries, whereas conductivity at higher frequencies is attributed to the conducting grains. Henceforth, we argue that conducting grains play an important role in high conductivity at higher frequencies. We also noted that the ac conductivity of Cr doped Mg–Zn Cobaltite is lower as compared to the $Mg_{0.5}Zn_{0.5}Co_2O_4$. It might be because of the existence of spinel-type and rocksalt-type structures. The spinel phase of Cr doped Mg–Zn Cobaltite is found to be unstable as reported earlier [39].

Real and complex modulus spectroscopy is an important technique to study the electrical transport phenomena of materials [40]. Compared to the Impedance spectroscopy, the complex modulus formulation has been found advantageous in terms of discrimination between electrode polarization and grain boundary conduction. Figure 8 shows the frequency dependence of the real modulus (M') at room temperature. It is characterized by the identical value at a lower frequency and shows an almost sigmoid increase as frequency increases [41]. This can be understood as; at lower frequency region electrode polarization is active and the charge carriers are able to move within a long-range regime under the influence of applied electric field [42]. The undoped Mg–Cr cobaltite shows a maximum value of M' and M'' ($\sim 14.29 \times 10^{-5}$ and 6.05×10^{-4} respectively) at high frequency [43]. The inset view of Fig. 8 explains the imaginary modulus (M'') plot alongside the frequency at room temperature. Further, the irregularity observed in M''_{max} is indicating the existence of stretched exponent parameter (β) to decide the type of relaxation process within a material, i.e. Debye or non-Debye-type relaxation. The calculated β values are tabulated in Table 3. The β values for all the samples turned

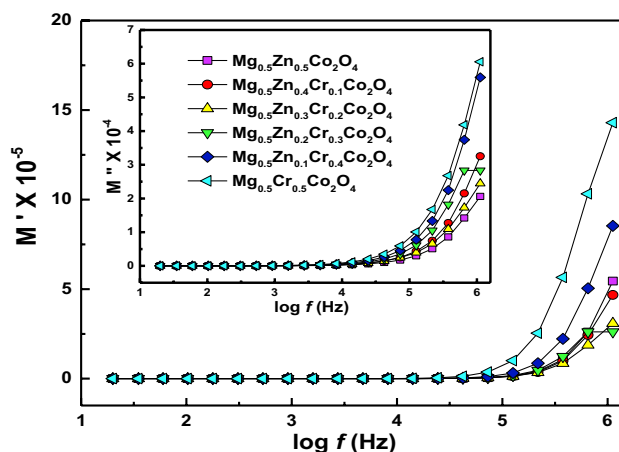


Fig. 8 Frequency dependence real part (M') and (inset view) frequency dependence imaginary part (M'') of electric modulus of $Mg_{0.5}Zn_{0.5-x}Cr_xCo_2O_4$ ($0.0 \leq x \leq 0.5$) at room temperature

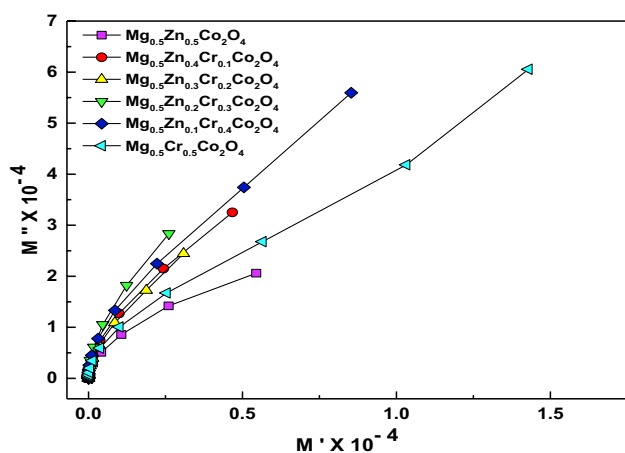


Fig. 9 Plot of M' vs M'' of $\text{Mg}_{0.5}\text{Zn}_{0.5-x}\text{Cr}_x\text{Co}_2\text{O}_4$ ($0.0 \leq x \leq 0.5$) at room temperature

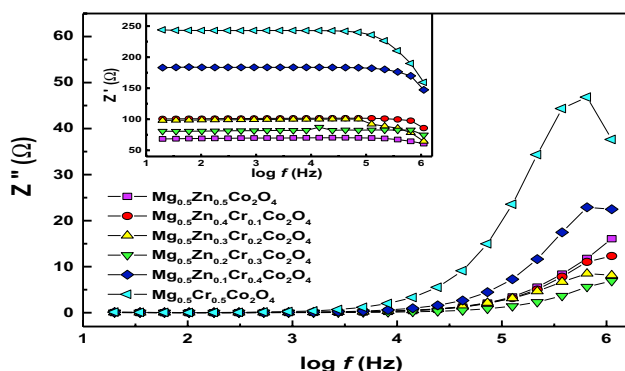


Fig. 10 Frequency dependent Reactive impedance (Z'') and (inset view) frequency dependence resistive impedance (Z') of $\text{Mg}_{0.5}\text{Zn}_{0.5-x}\text{Cr}_x\text{Co}_2\text{O}_4$ ($0.0 \leq x \leq 0.5$)

out to be less than unity. The fact that β values are less than unity shows the non-Debye nature of the samples [44]. To support this data, we have also plotted the variation of M' against M'' , which is depicted in Fig. 9. All the samples do not show any semi-circle type behavior, which indicates that only grain capacitance is dominant and the grain boundary modulus is out of the measurement scale as suggested earlier [41, 45].

The variation of the real part in the impedance (Z') as a function of frequency at room temperature for $\text{Mg}_{0.5}\text{Zn}_{0.5-x}\text{Cr}_x\text{Co}_2\text{O}_4$ ($0.0 \leq x \leq 0.5$) is shown in Fig. 10. The real part of impedance (Z') exhibits low-frequency dispersion due to polarization. At higher frequencies, all the curves merge together, which is attributed to the space charge effect as a result of the lowering of barrier properties of the sample. This shows that the value of impedance is higher in the low-frequency region which gradually decreases for the increase of Zn ion (as shown in inset of Fig. 10). In order to

make a better understanding of this space charge effect and the relaxation processes, the variation in the imaginary part of impedance (Z'') with frequency for $\text{Mg}_{0.5}\text{Zn}_{0.5-x}\text{Cr}_x\text{Co}_2\text{O}_4$ ($0.0 \leq x \leq 0.5$) are plotted in Fig. 10. For all the compositions, the plots exhibit enhanced peaks, where imaginary impedance is maximum. It shows the existence of relaxation processes in these materials. These peaks also shift towards lower frequencies on increasing the Cr concentration along with broadening in the width of the peak. It explains an increase in bulk resistance. The dispersion curves appear to merge at high frequency, which is attributed due to the space charge polarization [43, 46]. We end up by commenting that the space charge effect increases significantly with an increment of Cr concentration. This leads to the relaxation of space charge polarization.

4 Conclusions

A series of Mg–Zn cobaltite with Zn ion replaced by Cr ion $\text{Mg}_{0.5}\text{Zn}_{0.5-x}\text{Cr}_x\text{Co}_2\text{O}_4$ ($0.0 \leq x \leq 0.5$) have been synthesized with a motivation to improve the dielectric response useful in energy storage devices. Single-phase is observed for Mg–Zn cobaltite. Increased Cr ion leads to new phases (Co_3O_4 , Cr_2O_3) in mixed $\text{Mg}_{0.5}\text{Zn}_{0.5}\text{Co}_2\text{O}_4$. Rietveld refinement also confirms the existence of other phases in $\text{Mg}_{0.5}\text{Zn}_{0.5-x}\text{Cr}_x\text{Co}_2\text{O}_4$ ($x = 0.3, 0.5$). The crystallite size, as obtained by SXR D although reduced when compared to lab XRD, does not witness a systematic trend with enhanced Cr_2O_3 doping. The FTIR spectra of calcined cobaltites samples show two strong peaks with a medium amplitude around 665 and 563 cm^{-1} that are assigned to the stretching and vibrations of metal–oxygen bond in the sample. The shifting of these bonds towards the lower wave number is also observed, which indicates the increase in bond length.

The $\text{Mg}_{0.5}\text{Zn}_{0.5-x}\text{Cr}_x\text{Co}_2\text{O}_4$ ($x = 0.3$) shows the higher value of ϵ' . The value of ϵ' and $\tan \delta$ show a decreasing trend with increasing frequency. The highest dielectric constant is observed for Cr doped Mg–Zn cobaltite $\sim 1.07 \times 10^5$ for $x = 0.3$ with the lowest crystallite size (~ 29.16 nm). These small grains act as a large insulating barrier for the mobile charge carriers. The Cole–Cole plot of all the samples does not show any semi-circles type of behavior, which shows that only grain capacitance is dominant.

Acknowledgements UGC-DAE-CSR, as an institute is acknowledged for extending its facilities and financial assistance. Thanks to Dr. A. K. Sinha of RRCAT, Indore for providing SXR D facility. Dr. M. Gupta, Dr. D. M. Phase, Dr. V. Ganesan of UGC-DAE-CSR, Indore and Dr. Pratibha Sharma of School of Chemical Science, Devi Ahilya University, Indore are gratefully acknowledged for fruitful discussions. Authors are also thankful to Late Dr. Dinesh Varshney, for his support and encouragement.

References

1. R. Wang, X. Xue, W. Lu, H. Liu, C. Lai, K. Xi, Y. Che, J. Liu, S. Guo, D. Yang, *Nanoscale* **7**, 12833 (2015)
2. J. Xu, L. Wang, J. Zhang, J. Qian, J. Liu, Z. Zhang, H. Zhang, X. Liu, *J. Alloys Compd.* **688**, 933 (2016)
3. L. Cui, L. Huang, M. Ji, Y. Wang, H. Shi, Y. Zuo, S. Kang, *J. Power. Sources* **333**, 118 (2016)
4. X. Wang, G. Zhai, H. Wang, *J. Nanopart. Res.* **17**, 339 (2015)
5. A. Lakehal, B. Bedhief, A. Bouaza, H. Benhebal, A. Ammari, C. Dalache, *Mater. Res.* **21**, e20170545 (2018)
6. A. Stella, N. Soundararajan, K. Ramachandran, *AIP Adv.* **5**, 087104 (2015)
7. K. Yedluri, H.J. Kim, *RSC Adv.* **9**, 1115 (2019)
8. Q. Wang, B. Yu, X. Li, L. Xing, X. Xue, *J. Mater. Chem. A* **4**, 425 (2016)
9. L. Cui, L. Huang, M. Ji, Y. Wang, H. Shi, Y. Zuo, *J. Power Sources* **333**, 118 (2016)
10. S.G. Krishnan, M.V. Reddy, M. Harilal, B. Vidyadharan, I.I. Misnon, M.H.A. Rahim, J. Ismail, R. Jose, *Electrochim. Acta* **161**, 312 (2015)
11. Y. Kotani, R. Ise, K. Ishii, T. Mandai, Y. Oaki, S. Yagi, H. Imai, *J. Alloys Compd.* **739**, 793 (2018)
12. P. Thakur, A. Kool, B. Bagchi, S. Das, P. Nandya, *Phys. Chem. Chem. Phys.* **17**, 1368 (2015)
13. M. Baskey, R. Maiti, S.K. Saha, D. Chakravorty, *J. App. Phys.* **115**, 094306 (2014)
14. A. Tamilselvan, S. Balakumar, M. Sakar, C. Nayek, P. Murugavel, K.S. Kumar, *Dalton Trans.* **43**, 5731 (2014)
15. R.S. Pandav, R.P. Patil, S.S. Chavan, I.S. Mulla, P.P. Hankare, *J. Magn. Magn. Mater.* **417**, 407 (2016)
16. A. Yadav, M.A. Dar, P. Choudhary, P. Shah, D. Varshney, *AIP Conf. Proc.* **1728**, 020301 (2016)
17. L.B. McCusker, R.B. Von Dreele, D.E. Cox, D. LoueÈr, P. Scardi, *J. Appl. Cryst.* **32**, 36 (1999)
18. A. Pendashteh, J. Palma, M. Anderson, R. Marcilla, *Appl. Catal. B* **201**, 241 (2017)
19. R.D. Shannon, *Acta Cryst.* **32**, 751 (1976)
20. M.R. Panda, R.N. Bhowmik, H. Singh, M.N. Singh, A.K. Sinha, *Mater. Res. Express* **2**, 036101 (2015)
21. R. Bajaj, M. Sharma, D. Bahadur, *Dalton Trans.* **42**, 6736 (2013)
22. P.J. Lu, W.E. Fu, S.C. Huang, C.Y. Lin, M.L. Ho, Y.P. Chen, H.F. Cheng, *J. Food Drug Anal.* **26**, 628 (2018)
23. S. Hcini, A. Omri, M. Boudard, M.L. Bouazizi, A. Dhahri, K. Touileb, *J. Mater. Sci.* **29**, 6879 (2018)
24. G. Aravind, M. Raghassudha, D. Ravinder, R.V. Kumar, *J. Magn. Magn. Mater.* **406**, 110 (2016)
25. N.N. Binitha, P.V. Suraja, Z. Yaakob, M.R. Resmi, P.P. Silija, *J. Sol–Gel. Sci. Technol.* **53**, 466 (2010)
26. A.D. Jagadale, V.S. Kumbhar, R.N. Bulakhe, C.D. Lokhande, *Energy* **64**, 23 (2014)
27. C. Stella, N. Soundararajan, K. Ramachandran, *AIP Adv.* **5**, 087104 (2015)
28. K.B. Modi, U.N. Trivedi, P.U. Sharma, V.K. Lakhani, M.C. Chhantbar, H.H. Joshi, *Ind. J. Pure Appl. Phys.* **41**, 165 (2006)
29. İ Şabikoğlua, L. Paral, O. Malina, P. Novak, J. Kaslik, J. Tucek, J. Pechousek, J. Navarik, O. Schneeweiss, *Prog. Nat. Sci.* **25**, 215 (2015)
30. S. Nasri, A.L.B. Hafsia, M. Tabellout, M. Megdiche, *RSC Adv.* **6**, 76659 (2016)
31. K. Verma, A. Kumar, D. Varshney, *J. Alloys Compd.* **526**, 91 (2012)
32. T.G. Lupeiko, I.B. Lopatina, I.V. Kozyrev, L.A. Derbaremdiker, *Inorg. Mater.* **28**, 481 (1992)
33. R.S. Devan, B.K. Chougule, *J. Appl. Phys.* **101**, 014109 (2007)
34. K. Singh, N.S. Negi, R.K. Kotnala, M. Singh, *Solid State Commun.* **148**, 18 (2008)
35. G. Dhir, P. Uniyal, N.K. Verma, *J. Supercond. Nov. Magn.* **27**, 1569 (2014)
36. G. Kooops, *Phys. Rev.* **83**, 121 (1951)
37. A.K. Singh, T.C. Goel, R.G. Mendiratta, O.P. Thakur, C. Prakash, *J. Appl. Phys.* **91**, 6626 (2002)
38. N.H. Vasoya, P.K. Jha, K.G. Saija, J.A. Bhalodia, K.B. Modi, *J. Adv. Dielectr.* **7**, 1750022 (2017)
39. N. Kamioka, T. Ichitsubo, T. Uda, S. Imashuku, Y. Taninouchi, E. Matsubara, *Mater. Trans.* **49**, 824 (2008)
40. K. Kumari, A. Prasad, K. Prasad, *Am. J. Mater. Sci.* **6**(1), 1–18 (2016)
41. P. Saxena, D. Varshney, *J. Alloys Compd.* **705**, 320 (2017)
42. P.B. Macedo, C.T. Maynihan, R. Bose, *Phys. Chem. Glasses* **13**, 171 (1972)
43. A. Bagum, M.B. Hossen, F.U.Z. Chowdhury, *Ferroelectrics* **494**, 19 (2016)
44. J.H. Joshi, D.K. Kanchan, M.J. Joshi, H.O. Jethva, K.D. Parikh, *Mater. Res. Bull.* **93**, 63 (2017)
45. M.B. Hossen, A.K.M.A. Hossain, *J. Adv. Ceram.* **4**, 217 (2015)
46. P.M. Sathyamoorthy, C. Md Gazzali, G. Murugesan, Chandrasekaran, *Mater. Res. Bull.* **53**, 169 (2014)

Publisher's Note Springer Nature remains neutral with regard to jurisdictional claims in published maps and institutional affiliations.